Nanotechnology, Science and Applications

Dovepress
Taylor & Francis Group

Open Access Full Text Article

ORIGINAL RESEARCH

Trans-Cinnamaldehyde-Driven Silver Nanoparticles: Dual Role in Targeting Biofilm Disruption and Control of Biofilm-Forming Pathogens via Impairing Ferrous Ion Uptake

Patryk Strzelecki[1,2], Tom Ferté[2], Tomasz Klimczuk[3], Anna Zielińska-Jurek[4], Agnieszka Szalewska-Pałasz[1], Dariusz Nowicki[1]

[1]Department of Bacterial Molecular Genetics, University of Gdansk, Gdansk, Poland; [2]Institut de Physique et Chimie des Matériaux de Strasbourg, Université de Strasbourg, Strasbourg, France; [3]Department of Solid State Physics, Gdansk University of Technology, Gdansk, 80-233, Poland; [4]Department of Process Engineering and Chemical Technology, University of Technology, Gdańsk, Poland

Correspondence: Dariusz Nowicki, Department of Bacterial Molecular Genetics, University of Gdansk, Wita Stwosza 59, Gdansk, 80-308, Poland, Tel +48 585236065, Email dariusz.nowicki@ug.edu.pl

Purpose: Biofilm-related infections, especially those associated with medical devices like catheters, pose significant clinical challenges due to their resistance to conventional treatments. This study investigates a green chemistry-based approach to synthesize silver nanoparticles (AgNPs) stabilized with trans-cinnamaldehyde (*t*-CA) and evaluates their potential for combating microbial biofilms and based on novel mechanism of action.

Methods: Silver nanoparticles (*t*-CA-AgNPs) were synthesized using *t*-CA as both a reducing and stabilizing agent. The NPs were then thoroughly characterized using UV-Vis spectroscopy, X-ray diffraction (XRD), electron microscopy (TEM, SEM, STEM), and dynamic light scattering (DLS). We evaluated its antimicrobial potential against the most prevalence biofilm-forming pathogens including *Pseudomonas aeruginosa, Escherichia coli* and *Candida albicans* using minimal inhibitory concentration (MIC) and minimal bactericidal concentration (MBC) assays. Moreover, we investigated the mechanism of action of *t*-CA-AgNPs underlying biofilm inhibition. Biofilm formation and structure were verified by SEM imagining.

Results: DLS analysis confirmed that *t*-CA-AgNPs had an average particle diameter of 2.5 nm, coupled with a notably negative zeta potential (−45 mV), indicative of good colloidal stability. *t*-CA-AgNPs displayed potent antimicrobial properties, with MIC values ranging from 26 to 412 µg/mL and MBC values from 103 to 825 µg/mL. Biofilm formation inhibitory properties reached 88.74% of inhibition for *P. aeruginosa* and 70.60% for *E. coli*. Moreover, we found potent metal ion-chelating capabilities, importantly, in binding and reducing ferrous ions, the crucial factor of biofilm formation. Furthermore, *t*-CA-AgNPs substantially impaired biofilm development on catheter surfaces, underscoring their robust antibiofilm potential.

Conclusion: Presented here *t*-CA-AgNPs exhibit significant antimicrobial and antibiofilm activity. By effectively targeting critical elements in biofilm formation, such as ferrous ions, coupled with antimicrobial potential of both active compounds, these green-synthesized NPs have potential applications in significantly improving the safety and effectiveness of medical devices. However, further studies are needed to ensure their efficacy in clinical use.

Keywords: cinnamaldehyde, biofilm, AgNPs, silver nanoparticles, antimicrobial, green synthesis, iron uptake

Introduction

Antibiotic resistance is a significant global health concern. As a result, bacterial infections become harder to treat, potentially leading to more severe illnesses, prolonged hospital stays, and even death.[1] This problem is amplified by the multicellular, difficult-to-treat structures produced by microorganisms.[2] Biofilms are hot-spots for the emergence of resistant mutants, genetic transfer of mobile elements and a source of antimicrobial tolerance.[3] The formation and

Received: 24 May 2025
Accepted: 7 August 2025
Published: 18 September 2025

maintenance of biofilms are highly dependent on environmental cues, among which iron availability plays a pivotal role.[4] Iron is essential for bacterial metabolism, redox balance, and virulence factor expression. However, within the host, iron is tightly regulated and sequestered by proteins such as transferrin and lactoferrin, creating an iron-limited environment, and host nutritional immunity, that pathogens must overcome to establish infection.[4,5] Thus, the development of novel antibiofilm agents is of critical importance.[2,6]

In this context, nanoparticles (NPs), due to their unique physicochemical properties, hold potential in a wide range of applications, including targeted drug delivery, diagnostic imaging, and as antimicrobial agents.[7,8] This diverse range of characteristics empowers nanoparticles to fulfill a multitude of roles across various fields and industries.[9] Silver nanoparticles (AgNPs) have emerged as potent antimicrobial agents due to their broad-spectrum activity and ability to target bacterial cells through multiple mechanisms, including membrane disruption, production of reactive oxygen species (ROS), and interaction with bacterial DNA. Notably, AgNPs have been successfully employed in medical devices, wound dressings, and other biomedical applications to prevent bacterial infections. A detailed analysis of nanotechnology-based products indicated that 2000 items containing nano-sized materials, produced by over 600 companies, are being globally utilized across 32 countries.[10] The current global nanomaterials market accounted for USD 10.34 billion in 2020 and is anticipated to grow to USD 38.17 billion by 2029 at a compound annual growth rate (CAGR) of 17.8% throughout the 2021–2029 period.[11]

The method used for NP synthesis is crucial, as it dictates the final properties of the nanoparticles, such as size, shape, stability, and bioactivity.[12–14] A reliable and scalable method is needed to produce NPs in larger quantities, which is essential for industrial applications. Consistent and reproducible synthesis processes are vital to ensure that the NPs can be reliably manufactured to meet quality and performance standards.[9,12,13] Green synthesis of NPs, utilizing biocompatible and renewable resources, provides a solution to these concerns due to natural sources like plant extracts, microbes, or other bio-based materials.[10] Such an approach aims to minimize the use of hazardous chemicals and energy-intensive procedures associated with conventional NP synthesis methods.[15] However, the green methods are often burdened with low throughput or complex procedures, eg based on the growth and development of organisms, which limits scalability.

Trans-cinnamaldehyde (*t*-CA), a natural compound found predominantly in cinnamon essential oil (EO), is an excellent candidate for the purpose of NPs green synthesis due to its biocompatibility and multifunctional bioactivity[16,17] *t*-CA (3-phenyl-2-propenal) is derived from the bark of cinnamon trees (*Cinnamomum verum* or *Cinnamomum cassia*) and valued for its distinctive aromatic flavor and scent.[18] This powerful component of EO not only imparts the characteristic aroma of cinnamon spice but also offers a unique array of health beneficial properties. Among these are its noteworthy antioxidant capabilities, which aid in combating oxidative stress, its potent anti-inflammatory attributes that help alleviate various inflammatory conditions,[19] and its intriguing potential as an anticancer agent, showing promise in the field of cancer prevention and treatment.[20] Furthermore, *t*-CA's inherent antibacterial potency[16,21] adds to its versatility, finding utility across the culinary, cosmetic, and agricultural applications. In addition to these advantages, *t*-CA activity has been also demonstrated in NPs composition, either improving stability or enhancing their biological properties.[22,23]

In this study, we present a novel approach for the green synthesis of silver nanoparticles employing *t*-CA as a substrate to produce nanomaterial with desirable physicochemical properties and antimicrobial potential. We investigated the antimicrobial and antibiofilm potential of *t*-CA-AgNPs against clinically relevant pathogens, with a particular focus on their novel iron-chelating activity as a mechanism underlying biofilm inhibition.

Materials and Methods

Materials

Ultra pure water (ddH_2O Milli-q) from MilliQ pure water system (Merck Millipore, Germany) was used for synthesis experiments. The following substrates were used to NPs production: *t*-CA (97%, C80687, Sigma, Germany), analytical grade silver nitrate ($AgNO_3$, POCH, Avantor Performance Materials, Poland). pH adjustment was provided using analytical grade sodium hydroxide (NaOH, POCH, Avantor Performance Materials, Poland). Other relevant chemicals and microbiological broths have been indicated in the respective method descriptions below.

Methods

Green Synthesis of Silver Nanoparticles

The NPs synthesis was essentially conducted as described previously,[24,25] with some modifications. Briefly, the process of synthesis of *t*-CA-AgNP was conducted in a dark condition. Initially, 100 mL of water adjusted to pH 12 (NaOH) and then heated to 90°C. Next, *t*-CA (97%, C80687, Sigma, Germany) was then added to the solution to a final concentration of 0.5 mM. Following this, 500 µL of 0.1 M $AgNO_3$ water solution (ddH_2O) was carefully introduced dropwise into the mixture under constant stirring for 5 minutes to ensure thorough mixing and reaction. The resulting *t*-CA-AgNP solution was left to stabilize overnight at room temperature. The solution was then centrifuged at 2500 rpm, 20°C for 12 hours (Centrifuge 5810 R, Eppendorf, Germany) and stored at room temperature in a dark place.

t-CA-AgNPs Formation Monitoring

The formation of AgNPs and their optical properties of were analyzed spectrophotometrically using a UV-vis BioSpectrometer Kinetic instrument (Eppendorf, Germany). 10 nm Silver Nanospheres (nanoComposix, USA), 0.02 mg/mL stabilized on PVP was used as a standard material according to calibration curve. To measure the hydrodynamic diameter (HD), polydispersity (PDI) and potential charge of the *t*-CA-AgNPs suspensions, A Zetasizer Nano ZS (Malvern Panalytical, UK) was used.[26] The *t*-CA-AgNPs suspensions were diluted 1:100 with distilled water, sonicated for 15 min, and then transferred into U-type tubes before measurement with the Zetasizer at 25 °C.

XRD Analysis

The structural analysis of the synthesized AgNPs was conducted using the powder X-ray diffraction technique with the Xpert PRO-MPD (Panalytical, UK) diffractometer, equipped with a copper anticathode (λ Kα = 1.542 Å). The AgNP sample, which had been subjected to an air-drying process, was distributed in an even layer on a zero-background specimen silicon holder. Measurements were carried out in the 2θ angle range from 20 to 100 degrees, with a step size of 0.02 degrees and a scanning speed of 2.7 degrees per second. The size of the AgNP crystallites was further determined based on the Scherrer equation:

$$d = \frac{k\lambda}{\beta\ cos\theta}$$

Where k is the shape factor (for spherical structures, k=0.9); λ is the wavelength of the X-ray radiation (λ = 0.1542 nm); β is the experimental and theoretical (instrumental) full width at half maximum (FWHM) of the reflection occurring at angle θ. The analysis was performed for main five Bragg's reflections related to Ag.

Microscopic Evaluation

The electron microscopy method was employed to obtain information about the size, shape and dispersion of AgNPs. Scanning transmission electron microscopy (STEM) and scanning electron microscopy (SEM) analysis have been performed using Zeiss GeminiSem 500. *t*-CA-AgNPs were deposited on the grid and dried before the use.

FT-IR Spectroscopic Analysis

FT-IR spectra were recorded with wave numbers ranging from 400 to 4000 cm^{-1} for the *t*-CA-AgNPs, using IFS66 (Bruker, USA) spectrometer on KBr (pellet form) to record the IR spectra.

Determining of Interactions of t-CA-NPs with Metal Ions

Colorimetric detection was performed according to the procedure published by Hwa Kyung Sung et al.[27] Briefly, at room temperature a solution of *t*-CA-AgNPs (0.0185 mg/mL in ultrapure water) was prepared. Metal ion stock solutions (Cu^{2+}, Mn^{2+}, $Fe^{3}{}^{2+}$, Ca^{2+} in chloride form, and Zn^{2+} from sulfate monohydrate; trace metals grade, Sigma-Aldrich, Germany) were freshly prepared in ultrapure water. Aliquots (10µL) of the ion solutions (range of concentrations) were added stepwise to the 1mL *t*-CA-AgNPs suspension while gently mixing. After 5 min incubation at room temperature, the absorbance spectra were recorded using a BioSpectrometer (Eppendorf, Germany). Control measurements were performed for ion solutions without nanoparticles under identical conditions.

Ferric Reducing Antioxidant Ability (FRAP) Assay

The antioxidant capacity of the synthesized nanoparticles was evaluated using the Ferric Reducing Antioxidant Power (FRAP) assay based on Benzie and Strain with modifications.[28] A working solution was prepared by mixing 300 mM acetate buffer (pH 3.6), 10 mM ferric 2,4,6-tripyridyl-s-triazine (TPTZ, Supleco INC, USA), dissolved in 40 mM hydrochloric acid (HCl, POCH, Avantor Performance Materials, Poland), and 20 mM ferric chloride solution in a 10:1:1 ratio. Calibration curve was established with concentrations ranging from 100 to 1000 µM. For the assay, 100 µL of each sample or standard was mixed with 900 µL of the FRAP working solution and incubated 30 minutes in the dark at room temperature. The absorbance of the reaction mixtures was measured at 593 nm using a plate reader (Enspire, PerkinElmer, USA). Antioxidant capacity was calculated by interpolating the absorbance values of the samples against the standard curve. All experiments were performed in triplicate for accuracy. Negative controls were included to account for baseline readings.

Colorimetric Ferrozine-Based Assay

The ability of nanoparticles to chelate and reduce Fe ions was assessed using a modified FerroZine assay described by Jian Gong,[29] with dithiothreitol (DTT, Sigma Aldrich, Germany) as a reducing agent. A 1 mM FerroZine (sodium 4-[3-(2-pyridinyl)-5-(4-sulfophenyl)-1,2,4-triazin-6-yl]benzenesulfonate, Fluorochem, UK) solution was prepared in a 50 mM acetate buffer (pH 4.5) and stored in the dark at 4°C. $FeCl_3$ and $FeSO_4$ solutions (0.2–40 µM) were prepared to generate calibration curves. $FeCl_3$ was reduced to Fe^{2+} using DTT (final concentration: 20 mM) after 20 minutes of incubation. For the assay, 100 µL of Fe^{3+} solution was mixed in Eppendorf tubes with either 50 µL of *t*-CA-AgNP (in range of concentrations), 50 µL of deionized water (negative control), 50 µL of acetate buffer was added to each sample, followed by incubation at room temperature for 30 minutes. Samples were then centrifuged (13,000 RPM, 20 minutes), and DTT was added to the supernatant from *t*-CA-AgNPs, and to $FeCl_3$ samples to ensure complete Fe^{3+} reduction. Next, 200 µL of FerroZine solution was added to the samples, and the mixture was incubated for 10 minutes before measuring absorbance at 562 nm using a microplate reader (Enspire, PerkinElmer, USA). Chelation efficiency was calculated using the formula:

$$\text{Chelation percentage} = \left(1 - \frac{\text{Absorbance of sample}}{\text{Absorbance of negative control}}\right)\text{x}100$$

Microorganisms Growth Conditions

All microbial strains were plated on solid LB medium (Sigma-Aldrich, Germany) supplemented with 1.5% agar (Sigma-Aldrich, Germany) from the −80°C stock collection of our laboratory and incubated at 37°C for 20 hours. If liquid culture was required, the bacteria were incubated in LB Lennox (Sigma-Aldrich, Germany) broth at 37°C with shaking at 150 rpm, unless experimental conditions necessitated otherwise. All strains used in this study have been listed in Table S1.

Determination of MIC and MBC

The minimum inhibitory concentration (MIC) has been determined using the guidelines set forth by the British Society for Antimicrobial Chemotherapy (BSAC). A bacterial inoculum of approximately 10^6 colony-forming units per milliliter (CFU/mL) was tested against a range of compound concentrations spanning from 0.00644 to 1.64972 mg/mL. After 20 hours of incubation, all mixtures were plated onto LA medium to determine the number of CFU/mL, which allowed for the accurate determination of the MIC and minimum bactericidal concentration (MBC) values.

Quantification of the Bacterial Biofilm Biomass Reduction

To investigate the effect of *t*-CA-AgNPs on biofilm formation, overnight bacterial cultures were first diluted 1:100 in a fresh LA medium. Then, 100µL of the diluted inoculum was transferred to a sterile 96-well microtiter plate and incubated at 37°C for 48 hours, with *t*-CA-AgNPs added before the incubation period (t = 0). Once the bacteria had formed a biofilm, the culture medium was removed from the wells, and the biofilm was carefully washed with phosphate-buffered saline (PBS) to remove any unattached bacteria. The plate was then fixed by drying at 60°C for 1 hour. To stain

the biofilm, a 1% crystal violet solution was added to each well and left for 30 minutes. The excess crystal violet was removed by washing the plate with distilled water, and the plate was allowed to dry at room temperature. To extract the bound crystal violet, 33% acetic acid was added to each well, and the amount of 100µL crystal violet extracted from the biofilm was quantified by measuring the absorbance at 570 nm using an Enspire microplate reader (PerkinElmer, USA).

Cell Viability Assay

To assess the viability of bacteria in a culture, the 3-(4,5-dimethylthiazol-2-yl)-2,5-diphenyltetrazolium bromide assay (MTT) was performed. Overnight cultures of bacteria were first diluted 1:100 in LB medium and then transferred to a 96-well microtiter plate, which was then incubated at 37°C for 48 hours. After the incubation period, the medium was carefully removed, and fresh medium containing 0.1% MTT reagent in PBS was added to each well. The plate was then incubated for 2 hours at 37°C to allow the MTT reagent to be metabolized by viable cells. To solubilize the formazan crystals produced by viable cells, DMSO was added to each well, and the absorbance of each well was measured using an Enspire microplate reader, with the wavelength set to 570 nm.

Estimation of Biofilm Mass in Sterile Catheters

The experiment was conducted based on the protocol by Borowicz et al[30] with slight modifications. Bacteria were cultured at 25°C in YESCA medium (1 g/L yeast extract (Biomaxima, Poland) and 10 g/l casamino acids (Difco, USA) with shaking at 120 rpm overnight. The culture was then diluted to achieve a turbidity level of 4 McFarland units. The prepared suspension was further diluted at a ratio of 1:100. Sterile Nelaton Catheters (Unomedical, UK) were cut into 10 cm fragments and connected to a syringe. The bacterial inoculum was then drawn into the syringe, ensuring that the final volume did not exceed 3 mL. The experimental sample consisted of bacteria inoculum with AgNPs at a concentration of 1 MIC and tubes preincubated with *t*-CA-AgNPs (70°C for 24h) prior to experiment. The positive control was represented by bacteria inoculum without additional factors, while the negative control consisted of syringe with sterile broth and the one with the addition of AgNPs. After introducing the appropriate mixture of the tested substances into the syringe, they were tightly sealed under sterile conditions. The prepared samples were incubated for 72 hours at 25°C. After this time, the catheters were opened and rinsed with 20 mL of distilled water. After rinsing, a 1% solution of crystal violet was introduced and incubated at room temperature for 20 minutes. Then, the catheters were rinsed with distilled water until the unbound crystal violet was removed, and the catheters were photographed. Subsequently, a 33% solution of acetic acid in a volume of 2 mL was introduced into the catheters, and they were incubated under the same conditions. The absorbance of the solutions was then evaluated spectrophotometrically (BioSpectrometer, Eppendorf, Germany) at a wavelength of 570 nm.

CAS Assay for Iron Chelation

A modified Chrome Azurol S (CAS) assay based on[31,32] was used to examine the iron-chelating ability. The CAS dye solution was prepared by dissolving Chrome Azurol S (POL-AURA, Polska) to final concentration of 2 mM in deionized water, followed by the addition of a $FeCl_3$ solution (10 µM in 10 mM HCl) and a 10 mM hexadecyltrimethylammonium bromide (HDTMA, Sigma-Aldrich, Germany) solution in a 1:1:1 ratio. The final CAS dye solution was stored at 4°C. Then, 100 µL of CAS dye solution was mixed with 100 µL of tested compound. Controls included a negative control (CAS dye without nanoparticles) and a positive control (CAS dye with EDTA). Samples were incubated at RT for 5 hours. Samples were centrifuged (13000 rpm, 20 minutes) to make sure that nanoparticles do not affect the final results. Color change was visually assessed, and absorbance at 630 nm was measured using Enspire microplate reader (PerkinElmer, USA). Iron chelation activity (%) was calculated using the formula:

$$Iron\ Chelation\ Activity = \frac{A_r - A_s}{A_r} \text{x} 100$$

where A_r is the absorbance of the negative control, and A_s is the absorbance of the sample. The experiment was conducted in triplicate, and results were analyzed to determine nanoparticle iron depletion.

Statistical Analysis

T-test has been used for data analysis with normal distribution and equal variances, the Welch correction for unequal variances, and the U Mann–Whitney test for data without normal distribution. All differences between groups marked * - $P \leq 0.05$, ** - $P \leq 0.01$, *** - $P \leq 0.001$, **** - $P \leq 0.0001$. All experiments have been performed at least in triplicates.

Results and Discussion

t-CA-AgNPs Synthesis and Characterization

The use of phenolic extracts in the green synthesis of AgNPs offers an eco-friendly and sustainable alternative to traditional chemical methods.[24,25] These extracts act as reducing and stabilizing agents, leveraging their natural antioxidant properties to promote nanoparticle formation.[25,33] In this study, the plant secondary metabolite *t*-CA was successfully employed to synthesize AgNPs. The occurrence of NPs synthesis has been indicated by the change of color of the reaction mixture from transparent and colorless to dark orange. Next, the synthesis of *t*-CA-AgNPs was confirmed by UV–visible spectral analysis, showing a characteristic surface plasmon resonance peak at 411 nm (Figure 1A). The most effective synthesis was achieved under alkaline conditions (pH 12) at 90 °C. It was in line with other green synthesis studies where the bark extracts were used.[34,35] However, in our method the pure compound is used to formulate NPs instead of a crude extract, which may have favorable consequences for reproducibility and further application. *t*-CA-AgNPs formation was further confirmed in more detailed analysis. DLS analysis confirmed a narrow size distribution with a mean particle size of 2.61 nm (SD = 0.67 nm, PDI = 28.3%, xc = 2.5), with 99.1% of particles within this fraction, indicating uniformity of the synthesized nanoparticles (Figure 1B). The zeta potential distribution revealed a high negative surface charge, with a peak at –45 mV (mean = –41.8 mV, SD = 2.6 mV), which indicates strong electrostatic repulsion between particles (Figure 1C). Noteworthy, no significant change in UV-vis spectra has been observed at least for the 6 months (Figure S1), which is in line with the zeta potential observations. Stability of nanomaterials is considered as critical for maintaining effectiveness and consistent antibacterial activity, particularly in complex environments such as blood or tissue, where aggregation could otherwise reduce efficacy.

Then, atomic and molecular structure was determined by a powder X-Ray diffraction (pXRD). Small size of the NPs is reflected by substantial broadening of the XRD reflections. Figure 2A presents the pXRD pattern of the AgNP sample along with LeBail analysis conducted using the FullProf package.[36] The solid red line represents the theoretical XRD spectrum fitted to the experimental results, which are depicted by blue dots. Expected positions of Bragg reflections are marked with vertical lines, and Miller indices are placed above their corresponding diffraction reflections. The solid line at the bottom of the figure illustrates the difference between the model and the experimental results. LeBail analysis indicates that the broad reflections originate from the same phase with Fm-3m symmetry, for which the estimated lattice constant is a = 0.40888(7) nm. This is in very good agreement with literature data for metallic silver: a = 0.408626(4) nm,[37] 0.40862.[38] Narrow reflections of relatively low intensity, marked on the diffractogram with vertical arrows, stem

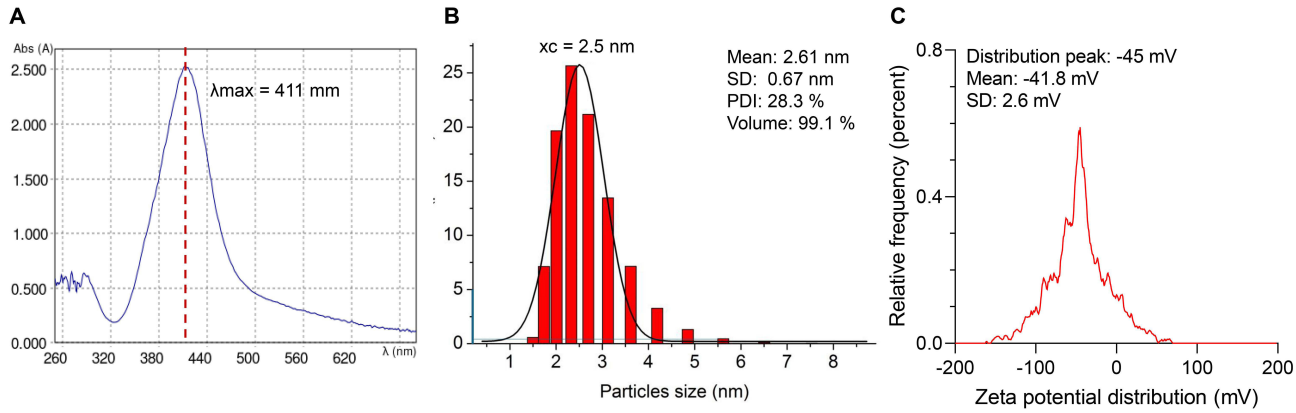

Figure 1 The physicochemical characteristics of *t*-CA-AgNPs. (**A**) The UV-vis spectra of *t*-CA-AgNPs after centrifugation and dilution 1:1000 - peak at 411nm (red dashed line), (**B**) Size and distribution according to Dynamic Light Scattering analysis, (**C**) Zeta potential distribution spectra.

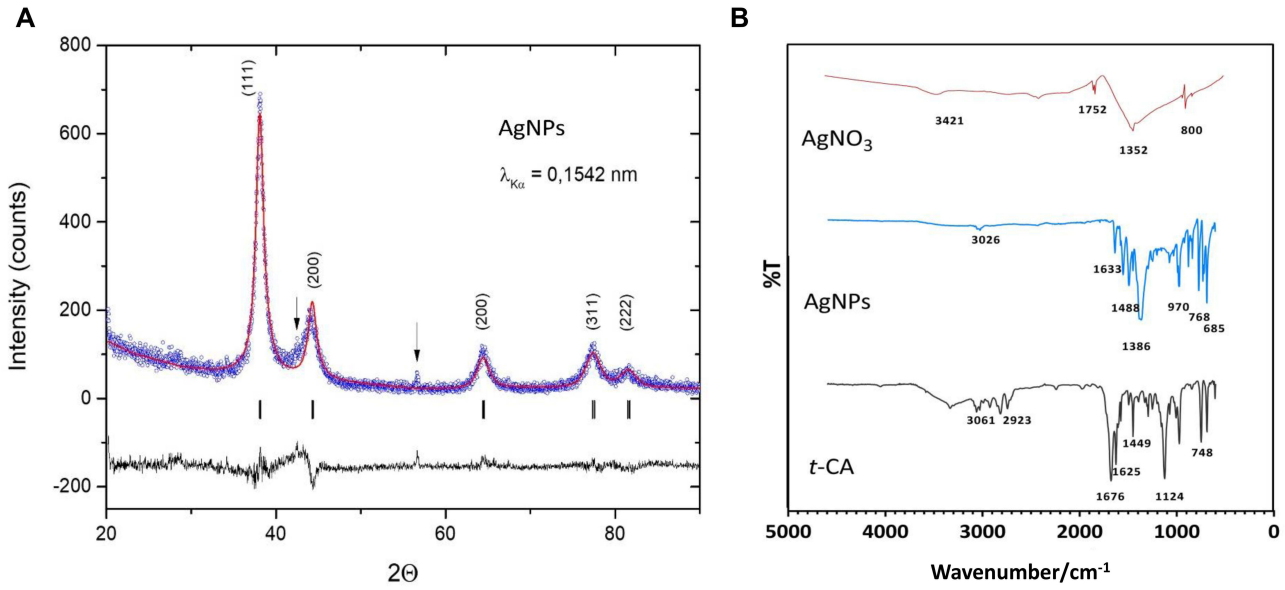

Figure 2 (**A**) Atomic and molecular structure determined by X-Ray diffraction. The size of AgNP crystals was determined based on the Scherrer equation. The analysis was conducted for five Bragg's reflections visible in the diffractogram (vertical dashes), and the calculated average value of the crystal diameter was 5.8 ± 0.5 nm, minor reflections were indicated by black arrows (**B**) FTIR analysis of $AgNO_3$, *t*-CA, and *t*-CA-AgNPs.

from an unknown phase. The analysis was performed for five reflections visible on the diffractogram (Figure 2A), and the calculated average crystallite diameter was 5.8 ± 0.5 nm. In summary, powder X-ray diffraction technique confirmed that the obtained material is a nanocrystalline form of silver with a diameter of approximately 5.8 nm.

Next, The FTIR spectrum was recorded at 4000–400 cm^{-1}, at a resolution of 2 cm^{-1}. The main characteristic peaks for *t*-CA derived NPs were found at 1633, 1488, 1386, 970, 768, 685 cm^{-1}, as presented on Figure 2B. The absorption peak at 1633 cm^{-1} is attributed to the C=C stretching vibrations of conjugated alkenes and aromatic rings, indicating the presence of unsaturated hydrocarbon structures derived from *t*-CA on the surface of the AgNPs. The peak at 1488 cm^{-1} corresponds to the aromatic C=C stretching vibrations, confirming the retention of the phenyl ring from *t*-CA in the NP composition. A notable peak at 1362 cm^{-1} is assigned to the symmetric stretching vibrations of carboxylate ions (COO^-). The presence of NaOH in the reaction mixture suggests that *t*-CA underwent partial oxidation to form cinnamic acid, which deprotonated under basic conditions to yield carboxylate ions. This indicates that side reactions occurred during the synthesis, leading to the formation of carboxylate groups that may act as dominant capping agents giving the molecule a strong negative surface charge. The band observed at 685 cm^{-1} is associated with metal–oxygen (Ag–O) stretching vibrations, suggesting interactions between silver atoms and oxygen-containing functional groups on the NP surface. This implies that oxygen atoms from oxidized *t*-CA or its derivatives eg, cinnamic acid, are coordinating with the silver NPs, contributing to their stabilization.

Finally, we observed NPs through different electron microscopy techniques (Figure 3A–C). In the TEM analysis (Figure 3A), the NPs appear as dark spots against a lighter background (bright field), showing a relatively uniform size distribution. The particles, mostly well-dispersed, are in the range of 10 nm, though some regions exhibit slight aggregation. The SEM study (Figure 3B) highlights the surface morphology of the NPs (secondary electrons). The particles are more densely packed and aggregated, forming a somewhat continuous layer. The individual particles are less distinct compared to the TEM image, but they are still within a similar size range, appearing roughly spherical. In the STEM observation (dark field) developed at 10 kV (Figure 3C), the NPs are more clearly defined with higher resolution. This technique reveals their spherical shape and shows them forming clusters or chains, indicating some level of interaction or assembly. The magnified view further details the internal structure of these particles. Overall, across all techniques, the NPs are consistently sized, roughly spherical, and exhibit moderate degrees of aggregation.

A critical advantage of our approach lies in the simplicity and reproducibility of the synthesis method. Unlike many green synthesis methods that rely on complex plant extracts, which contain an unpredictable mix of reducing agents, our

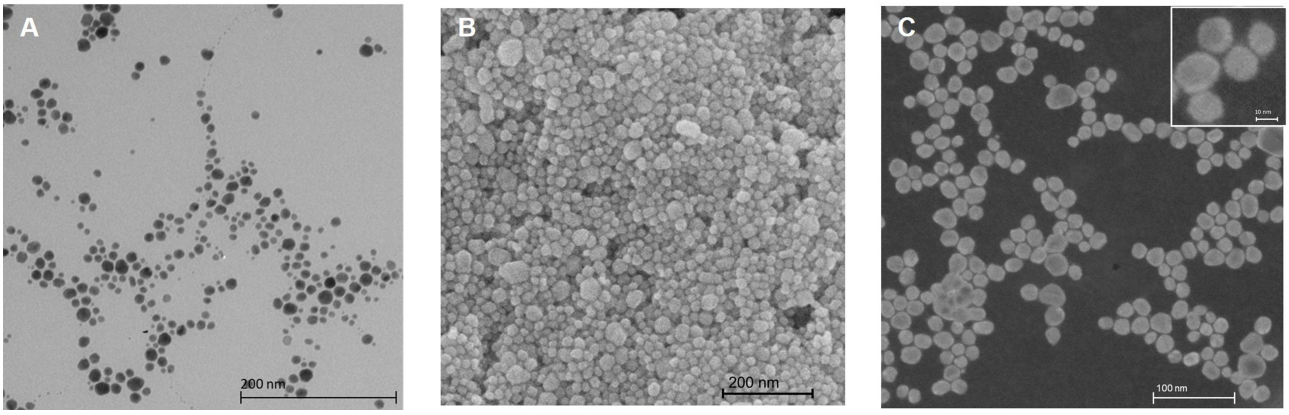

Figure 3 Visual representation of *t*-CA-AgNPs by (**A**) Transmission Electron Microscope, bar represents 200 nm (**B**) scanning electron microscope at 20 kV bar represents 200 nm, (**C**) scanning transmission electron microscope at 10 kV (bar represents 100 nm), magnified view with bar representing 10 nm to show exact size and shape of single *t*-CA-AgNPs.

method uses a single, well-defined compound.[39] This allows for greater control over the nanoparticle synthesis process, leading to uniform particle size, shape, and stability.

Metal Ions Sensing

Functionalized AgNPs are widely used as optical sensors for heavy metal ions in water as well as polluted environmental systems.[40] In Figure 4A we showed the results of a study designed to detect metal ions like Fe, Mn, Cu, Ca, and Zn by synthesized *t*-CA-AgNPs performed by UV-Vis absorption method. The different colored curves correspond to the absorbance spectra of *t*-CA-AgNPs in the presence of specific metal ions at concentrations as indicated. Absorbance peak at 411 nm characteristic for *t*-CA-AgNPs serves as a reference for evaluating the interactions with the metal ions. The introduction of metal ions causes changes in the intensity and position of this peak, indicating interactions between the AgNPs and the metal ions. For instance, the presence of copper ions results in a decrease in peak intensity and a slight right shift, suggesting aggregation or changes in the NPs' environment. Similar trends are observed for manganese and iron ions, with the iron ions showing the most significant effect, likely indicating strong interaction. Calcium and zinc ions also cause a decrease in absorbance and slight shifts, though to a lesser extent. Additionally, we performed the color analysis of the solutions to visually confirm the interaction of AgNPs with the different metal ions (Figure 4B). The

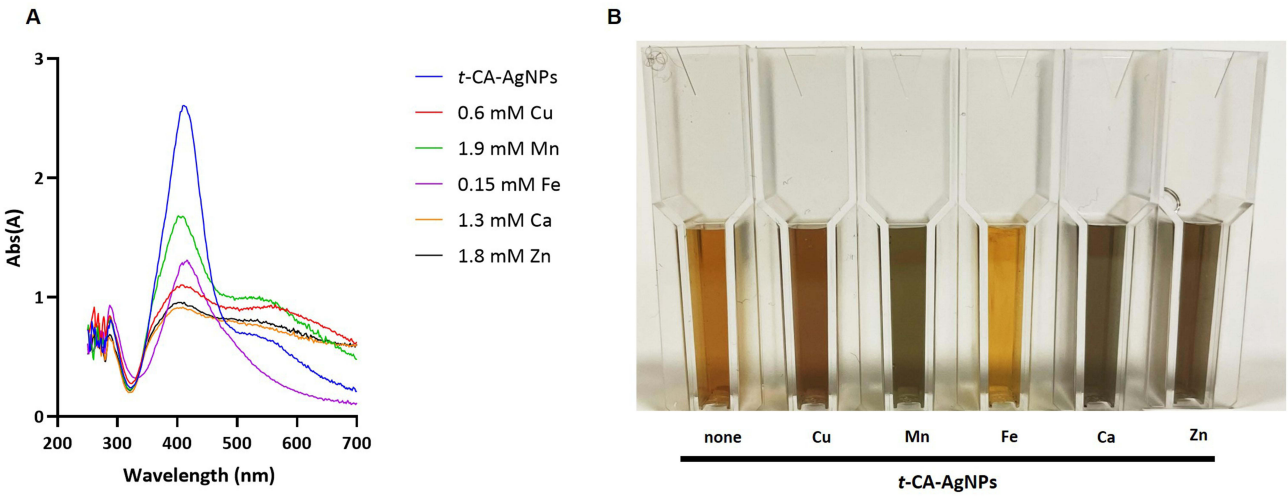

Figure 4 Visual and spectroscopic results of colorimetric detection of metal ions using *t*-CA-AgNPs. The absorption spectra (**A**) and corresponding solution colors (**B**) are shown for *t*-CA-AgNPs in the presence of different metal ions (at concentrations indicated): Cu^{2+}, Mn^{2+}, Fe^{2+}, Ca^{2+}, and Zn^{2+}.

solutions exhibit distinct color changes that align with the observed spectral shifts, serving as a practical confirmation of the colorimetric detection method. Changes in peak intensity suggest that metal ions induce NPs aggregation or alter the dielectric environment, which modifies the surface plasmon resonance. Overall, these results demonstrate that *t*-CA-AgNPs can effectively detect certain metal ions through changes in their optical properties, particularly for Fe and Cu ions, which show the most pronounced interactions, both spectroscopically and visually.

Antimicrobial Activity of t-CA-AgNPs

Susceptibility Tests

We conducted tests to evaluate the antibacterial efficacy of *t*-CA-AgNPs using the two-fold microdilution method to determine the minimum inhibitory concentration (MIC) and minimum bactericidal concentration (MBC) (Table 1). Both constituents, *t*-CA and silver nitrate, were tested individually in growth inhibition assays at the concentration used for nanoparticle synthesis (0.5 mM); however, neither compound exhibited measurable inhibitory effects against the investigated pathogens. The NPs were effective against all tested strains, with MIC values ranging from 0.026 to 0.412 mg/mL and MBC values ranging from 0.103 to 0.825 mg/mL. When compared to other natural antibacterial compounds, such as essential oils, plant extracts, or naturally derived antimicrobial peptides, the NPs exhibited a competitive or superior performance. For instance, many essential oils like tea tree or oregano oil have reported MIC values in the range of 0.05 to 2 mg/mL,[41,42] depending on the bacterial strain, while plant-derived compounds such as flavonoids often show MIC values ranging from 0.05 to 1 mg/mL.[43,44] *C. albicans* was the most sensitive to *t*-CA-AgNPs (MIC: 0.026 mg/mL), while *E. coli* KB17, KB18, and *Enterococcus faecalis* were the most resistant (MIC: 0.412 mg/mL). Notably, highly virulent strains such as *S. aureus* MRSA and *E. coli* ESBL required a higher concentration (0.825 mg/mL) to achieve MBC, compared to wild-type *E. coli* (0.412 mg/mL). These results align with literature, which suggest that fungi are generally more sensitive to silver NPs.[45] The observed effect is likely due to membrane disruption and the release of Ag^+ ions, which bind to cellular components such as proteins and polysaccharides.[46] The toxicity of synthesized NPs can be actively enhanced by the capping agent, as antibacterial activity of *t*-CA were broadly reported.[16] Moreover, it has been reported that NPs of smaller sizes offer a higher surface-area-to-volume ratio, which enhances the interaction between the NPs and bacterial cells.[47] This increased surface area facilitates more efficient attachment to bacterial cell walls, enhancing the bactericidal effect by releasing silver ions and generating reactive oxygen species (ROS). For instance, the 2.5 nm *t*-CA-AgNPs likely owe their strong antibacterial properties to this enhanced surface reactivity. Moreover, the antibacterial efficacy of *t*-CA-AgNPs is consistent with literature on AgNPs, which shows potent activity against both

Table 1 MIC and MBC Values for Representatives of Gram-Negative, Gram-Positive Bacteria and *Candida albicans*

Strain	MIC (mg/mL)	MBC (mg/mL)
E. coli MG1655	0.103	0.412
E. coli UTI89	0.240	0.470
E. coli CFT071	0.103	0.240
E. coli ESBL KR45	0.206	0.825
E. coli KB017	0.412	0.825
E. coli KB018	0.412	0.825
S. aureus ATCC 25923	0.052	0.206
S. aureus MRSA RA532	0.206	0.825
P. aeruginosa 6121	0.103	0.240
E. faecalis 773	0.412	0.825
L. monocytogenes BAA	0.206	0.412
C. albicans 222	0.052	0.412
C. albicans ATCC 2091	0.026	0.206
C. albicans 1750	0.026	0.103

Gram-positive and Gram-negative bacteria.[48] The slightly higher MICs observed for antibiotic-resistant strains like MRSA and *E. coli* clinical isolates could be due to their enhanced defense mechanisms, including biofilm formation and efflux pumps.[49,50]

Biofilm Formation

Biofilms are highly resistant to conventional antibiotics due to their protective extracellular matrix, altered metabolic state, and enhanced genetic exchange within the bacterial community. Testing antimicrobials on biofilms mimics conditions, such as these found in chronic infections and medical device contamination.[51] The effect of *t*-CA-AgNPs on biofilm mass formation was assessed using several Gram-negative and Gram-positive bacterial strains (Figures 5A and S2). Namely, three *E. coli* strains were tested: the wild-type MG1655 laboratory strain and two reference uropathogenic strains, UTI89 and CFT073, widely known for their potential to cause urinary tract infections (UTI).[52] *Pseudomonas aeruginosa* 6121 strain was included due to its ability to produce a significant, hard to eradicate biofilm mass and its role in nosocomial infections. Additionally, two Gram-positive strains, *Staphylococcus aureus* (ATCC 25923) and a clinical isolate of the MRSA variant, were evaluated. Our analysis revealed that *E. coli* MG1655, *S. aureus* ATCC 25923, and *P. aeruginosa* 6121 exhibited the highest percentages of biofilm reduction, with decreases of biofilm mass by 70.60%, 78.40%, and 88.74%, respectively. Notably, these substantial reductions indicate the strong biofilm-inhibiting properties of *t*-CA-AgNPs across both Gram-negative and Gram-positive bacterial species, including the notoriously difficult-to-treat *P. aeruginosa*. Interestingly, the MRSA strain of *S. aureus* showed biofilm reduction of 71.28%, which was not significantly different from the non-MRSA version. This finding implicates a substantial activity of *t*-CA-AgNPs even against resistant strains. For the uropathogenic strains, the *E. coli* UTI89 exhibited a moderate biofilm reduction of 56.11%, whereas the CFT073 strain proved to be the most resilient to *t*-CA-AgNPs treatment, with only a 23.87% reduction in biofilm mass. This notable variation between the UTI89 and CFT073 strains emphasizes the heterogeneity of biofilm-forming capacity and susceptibility within uropathogenic *E. coli* populations. To further investigate the efficacy of *t*-CA-AgNPs against *E. coli* strains associated with urinary tract infections, we expanded the analysis to a larger collection of uropathogenic *E. coli*[52] (UPEC, n=20) (Figure 5B). We observed a significant reduction in biofilm mass for the UPEC strains used, with a reduction factor of 0.45 ± 0.20 as shown in Figure 5B. These findings reinforce the potential of *t*-CA-AgNPs as a promising antimicrobial treatment, especially in biofilm-associated infections caused by UPEC.

Biocidal Effect on Biofilms

We further assessed the survival of cells within the established biofilm by performing an MTT assay (Figure 5C). A significant reduction in cell viability was observed in all tested strains. The most pronounced decrease in cell viability was seen in both *S. aureus* strains, with an 88.46% reduction in the MRSA strain and a 79.52% reduction in the *S. aureus* ATCC strain compared to the untreated group. *E. coli* MG1655 exhibited a 77.01% decrease in survival. The UTI89 and CFT073 strains showed similar decreases, with reductions of 65.04% and 66.72%, respectively. Thus, we conclude that *t*-CA-AgNPs treatment is effective in killing bacteria in formed biofilm, as decreased viability was higher than observed mass reduction for CFT073. Notably, *P. aeruginosa* exhibited the highest survival rate, with a decrease of 44.18% compared to untreated cells. The inhibitory effect of AgNPs treatment on bacterial biofilms were recently studied and highlight the aspect of biofunctionalization of nanomaterials at surfaces for controlling infections.[51] However, the mechanism of action underlying AgNPs antimicrobial activity and their molecular targets that lead to the death of bacterial cells remain undetermined.[14] To attempt that, we used the 2',7'-dichlorofluorescin diacetate (DCFDA) assay to assess ROS production as a potential bactericidal factor, but the treatment with *t*-CA-AgNPs did not lead to any increase in oxidative stress in cells (data not shown). *t*-CA is widely known for its antioxidant properties, which were previously showed by us and others.[17,21] On the other hand, we surprisingly found that *t*-CA-AgNPs has good Ferric Reducing Antioxidant Power (FRAP), combined with iron chelating capacity comparable to EDTA, as presented in Figure 6. Specifically, the nanoparticles were able to reduce up to 50 µM of ferrous iron at the highest tested concentration (12.5 µg/mL), while neither $AgNO_3$ nor *t*-CA alone exhibited such activity (Figure 6A and S5) (thus data regarding $AgNO_3$ and *t*-CA were not plotted on graph). To further evaluate iron-binding capacity we employed gold standard

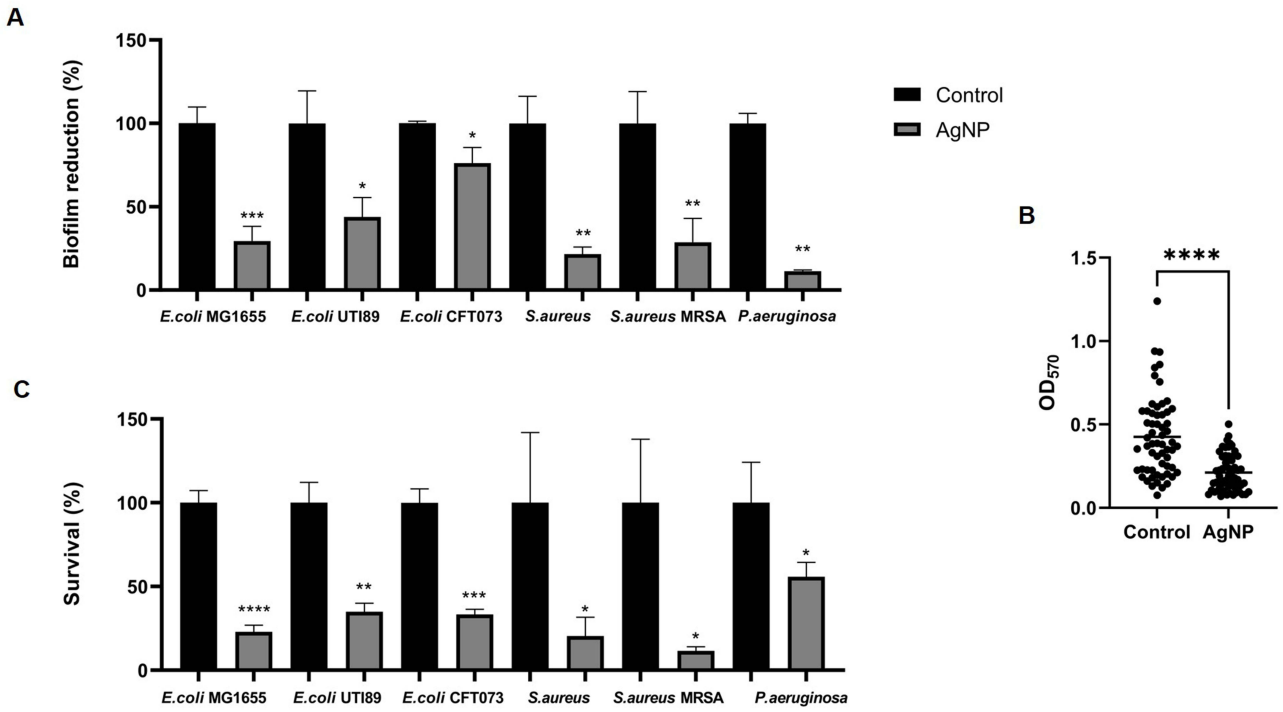

Figure 5 Biofilm mass measured by crystal violet binding in 96-well after a 72 h of incubation at 37°C in a microtiter plate for (**A**) 20 representatives of UPEC and series of (**B**) Gram-negative and Gram-positive bacteria (**C**) Survival of bacterial cells in formed biofilm. Statistical differences (Student's *t* test) between groups were marked as * - P ≤ 0.05, ** - P ≤ 0.01, *** - P ≤ 0.001, **** - P ≤ 0.0001.

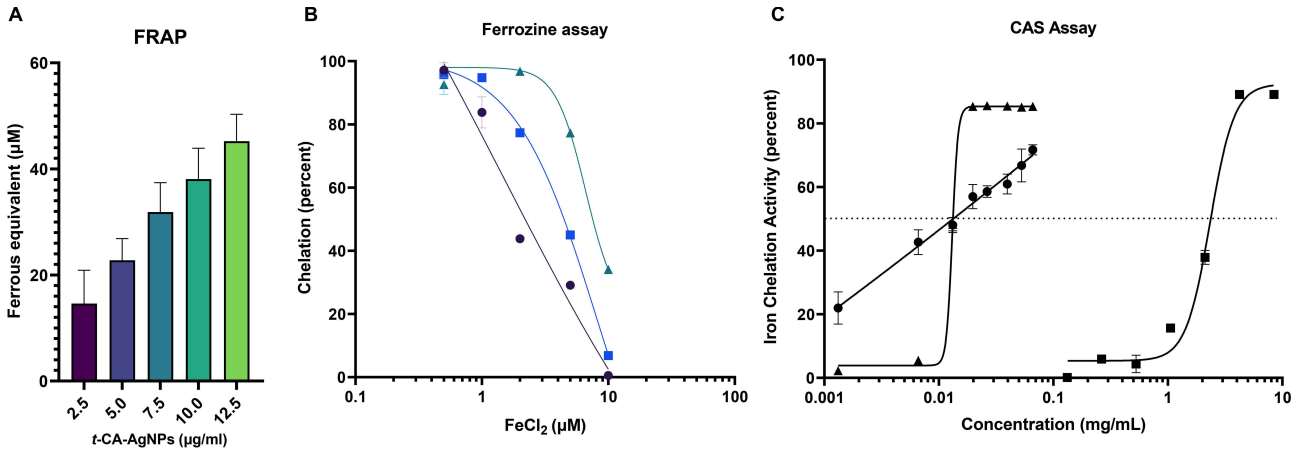

Figure 6 Iron-reducing and chelating properties of *t*-CA-AgNPs. (**A**) Reducing power of t-CA-AgNPs measured by FRAP assay, expressed as μM ferrous equivalents. (**B**) Ferrozine assay showing iron chelation (%) by *t*-CA-AgNPs (20, 40, 80 μg/mL, marked as green triangle, blue squares, violet circles respectively) in response to increasing concentrations of $FeCl_2$ (0.5–10 μM). (**C**) CAS assay assessing Fe^{2+} chelation by *t*-CA-AgNPs (circle), trans-cinnamaldehyde (square), and EDTA (triangle). Dose-dependent response curves were plotted, and data presented as means ± SD. All experiments were done in triplicates.

methods - ferrozine based assay (Figure 6B and S6) and Chrome Azurol S (CAS) assay (Figure 6C) - to assess Fe chelation ability of the tested agents.[53] In both assays the *t*-CA-AgNPs have proven to be effective in Fe ions chelation. The ability of Fe(III) binding tested in CAS assay showed 50% iron binding activity at 13.3 μg/mL for EDTA and 13.5 μg/mL for *t*-CA-AgNPs (Figure 6C). Notably, moderate chelating activity was also observed for *t*-CA alone, although at a much higher concentration of 2.37 mg/mL. Iron metabolism has emerged as a target for antimicrobial strategies aiming to disrupt biofilm integrity.[54,55] Agents that chelate iron or interfere with microbial iron acquisition systems can effectively impair biofilm formation and reduce pathogen viability.[56] Natural compounds like vanillin,

curcumin, ginkgolic acid, quercetin and many others have been shown to effectively chelate iron and mitigate bacterial infection.[57–59] As shown in our study, phenolic *t*-CA exhibits this potential as well (Figure 5C). More importantly, *t*-CA AgNPs derived on its basis exhibited multiply enhanced chelating properties compared to *t*-CA alone. *t*-CA is a volatile EO with poor water solubility, these features have been improved by formation of NP complex with Ag. The enhanced solubility and exhibition of *t*-CA molecules on Ag^0 core may have greatly affected these capacities. Recently, it has been proposed to use hybrid nanomaterial based on *Myrtus communis* extract MC-AgNP to reduce excess iron ions in a thalassemia model.[60] MC-AgNPs in the form of a colloidal solution demonstrates for chelating power of excess iron and improves pathological changes in iron overloaded mice. In another study, natural chelators have been tested to overcome *P. aeruginosa* and *S. aureus* infections and interfere with their virulence factors expression.[61] Potential additional effects of iron chelators on impregnated central venous catheters were well described in work by Itoh et al[62]

Determination of t-CA-AgNPs Antibiofilm Activity in Medical Catheters

Urinary catheters are critical medical devices commonly used to manage urinary retention and incontinence, especially in patients with neurological disorders. However, these catheters can also become conduits for microorganisms, facilitating their entry into the bladder and disrupting the urinary tract's innate defense mechanisms. This often leads to catheter-associated urinary tract infections (CAUTIs), which are among the most prevalent hospital-acquired infections.[63] In Figure 7, we assessed the effectiveness of *t*-CA-AgNPs in preventing biofilm formation on sterile Nelaton catheters, focusing specifically on their ability to inhibit microbial cell adhesion and biofilm development on medical devices. This evaluation was carried out through two distinct experimental approaches (Figures 7 and S3). In the first one, *t*-CA-AgNPs were directly introduced into the growth medium. This method led to significant reductions in biofilm formation, as indicated by the substantial decrease in biofilm mass of various bacterial strains. Notably, *E. coli* UTI89, *E. coli* CFT073, and *P. aeruginosa* exhibited reductions in biofilm mass of approximately 93%, underscoring the potent antimicrobial and anti-biofilm effects of *t*-CA-AgNPs in Gram-negative pathogens. Among the Gram-positive strains, the non-MRSA strain of *S. aureus* demonstrated a remarkable biofilm reduction of 91.65%, while the MRSA strain, though more resistant, still showed a significant reduction of 77.12%. These results highlight the strong biofilm-inhibitory properties of *t*-CA-AgNPs, even against methicillin-resistant bacteria.

In the second approach, sterile Nelaton catheters were pre-incubated with *t*-CA-AgNPs (0.103 mg/mL), allowing the nanoparticles to coat the catheter surface. The catheters were then air-dried to immobilize the nanoparticles. Even with this immobilization technique, we observed a consistent and notable inhibition of biofilm formation for all strains tested (Figure 7A). Although the reduction in biofilm mass was somewhat lower compared to the first approach, the differences were not statistically significant ($p > 0.05$), indicating that the immobilized *t*-CA-AgNPs were still highly effective in preventing biofilm formation on catheter surfaces (Figures 7A and S4).

Further analysis specifically focused on UPEC strains, as shown in Figure 7B. The average reduction in biofilm mass on catheters coated with *t*-CA-AgNPs was 62.69%, underscoring the potential of these NPs in significantly diminishing biofilm formation, even when challenged by highly virulent clinical isolates. This reduction is particularly noteworthy considering the recalcitrant nature of biofilms formed by UPEC, a major contributor to CAUTIs. The visual evidence presented in Figure 7C supports the quantitative data, demonstrating the effectiveness of *t*-CA-AgNPs treatment in reducing biofilm formation on catheters. The treated catheters show markedly less crystal violet staining, indicating significantly less biofilm mass compared to the untreated controls. These findings confirm the ability of the nanoparticles to effectively inhibit microbial adhesion and biofilm establishment on medical device surfaces. In recent years, comprehensive attempts have been made to address the problems associated with CAUTI.[64] The utility of AgNPs decorated materials is one of prominent solutions in this filed.[65] For instance, Prateeksha et al demonstrated the potential of chrysophanol-functionalized silver NPs as anti-adhesive and anti-biofouling coatings for urinary catheters, effectively preventing catheter-associated infections.[66] The efficacy of impregnated catheters relies on the release of free silver ions at antibacterial concentrations from both the internal and external surfaces.[67] Despite concerns regarding the potential neutralization of silver ions in urine by chloride ions and proteins, several approaches for incorporating silver into catheter materials have been explored.[65]

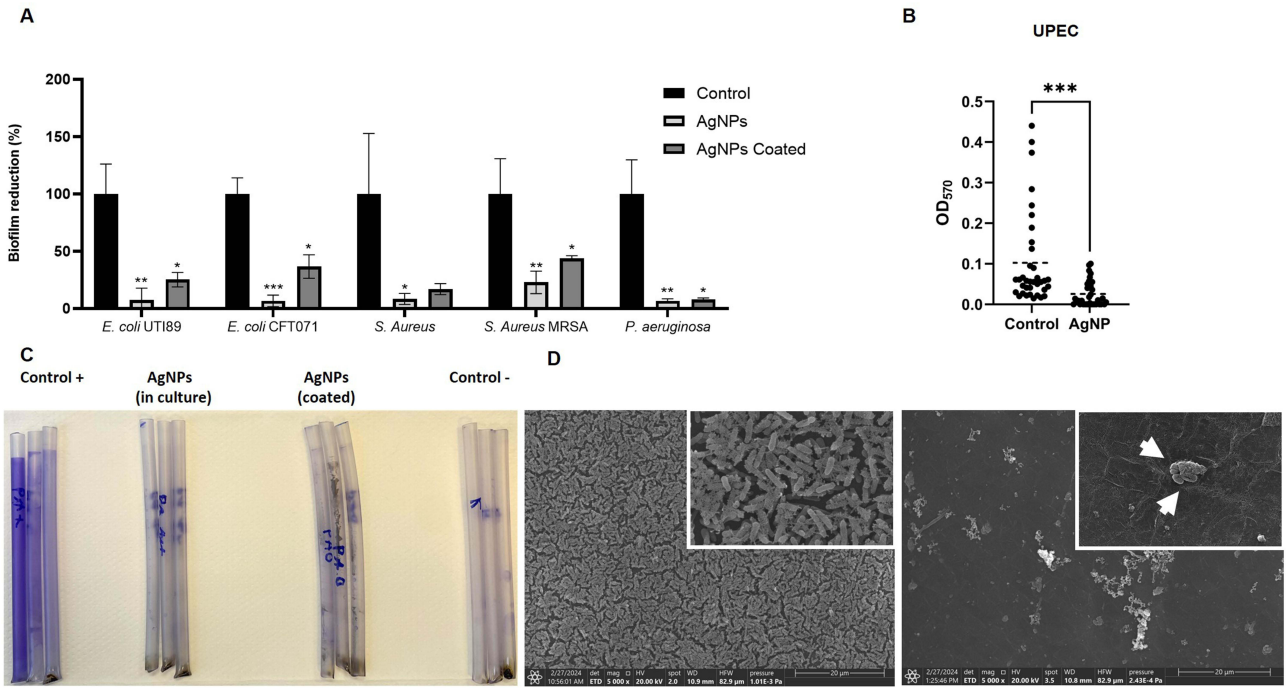

Figure 7 Biofilm mass measured by crystal violet binding in Nelaton Catheter (Unomedical) for a (**A**) series of Gram-negative and Gram-positive bacteria incubated in YESCA medium at 25°C (**B**) UPEC (**C**) binding of crystal violet by biofilm created by *Pseudomonas aeruginosa*, (**D**) Catheters under SEM microscope (left) untreated bacterial cells, (right) bacteria after incubation in catheter coated with AgNPs. Damaged cells with cytoplasmic leakage were marked with white arrowheads. Statistical differences (Student's *t* test) between groups were marked as * - P ≤ 0.05, ** - P ≤ 0.01, *** - P ≤ 0.001.

The use of bioactive agents like *t*-CA to produce NPs can impart additional and desirable properties to the materials. Herein, we provide a new perspective of green synthesized-AgNPs interactions as a selective ion chelators to mitigate microbial viability and biofilm development. It is of particular importance for preventing UPEC infection as these bacteria rely on the effective iron acquisition in the iron-limited environment of urine. Compared to traditional AgNP systems, the combination of *t*-CA with AgNPs offers synergistic effect, where AgNPs inherent bioavailability and net charge amplifies the bactericidal and anti-biofilm properties of *t*-CA. This dual action makes *t*-CA-AgNPs a promising candidate for biomedical applications, particularly in biofilm-associated infections where conventional treatments fail. The synergistic effect for cinnamon bark extract and AgNPs was previously reported.[68–70] For example, Gosh et al showed strong bactericidal action against spore forming *Bacillus cereus* and *Clostridium perfringens* by combination of AgNPs (25–40 nm size) and *t*-CA.[70] Moreover, in their work, Ram et al reported enhanced AgNPs action against MDR *E. coli* strains by entrapping *t*-CA into NPs composition.[69] That entrapment enhanced the efficacy of *t*-CA and AgNPs and was reported to be safe and efficient to treat infection in vivo in *G. mellonella*.

Despite the promising results presented in this study, further research is needed to fully evaluate the long-term stability, biocompatibility, and safety of *t*-CA-AgNPs through extensive in vivo studies, especially given their potential application in medical devices like urinary catheters. Moreover, future research should aim to optimize the dosage and delivery methods for clinical applications. While our study demonstrates the substantial reduction in biofilm formation achieved with *t*-CA-AgNPs, translating these findings to clinical settings will require a comprehensive assessment of their performance during in vivo studies.

Conclusions

In recent years, green-synthesized nanoparticles have demonstrated diverse bioactivities, including antioxidant, anticancer, antimicrobial, antiviral, and anti-inflammatory effects. Among them, silver nanoparticles have gained particular attention for applications in drug delivery, diagnostics, and infection control due to their broad-spectrum biological activity and eco-friendly profiles. In this study, we specifically aimed to evaluate the antimicrobial and antibiofilm

potential of *t*-CA-AgNPs. Our findings clearly demonstrate that this goal was achieved: the *t*-CA-AgNPs exhibited potent bactericidal activity with low MIC and MBC values across both Gram-positive and Gram-negative pathogens and significantly reduced biofilm biomass, including on clinically relevant urinary catheters. Interestingly, beyond the expected silver-mediated effects, we identified an additional mechanism of action based on iron sequestration, depriving bacteria of this key micronutrient required for biofilm formation and persistence. These results confirm that *t*-CA-AgNPs not only possess strong antimicrobial efficacy but also effectively disrupt biofilm development, directly addressing the challenge that motivated this study. The promising antiseptic and disinfectant activity observed on catheter surfaces highlights their translational potential for medical device protection. However, to fulfil the limitations of the study future work should focus on in vivo validation and safety assessment to pave the way for clinical application of this dual-action nanomaterial. In addition, the current experiments were performed under controlled laboratory conditions, and factors such as long-term stability in complex biological fluids, potential cytotoxicity to host tissues, and scalability of the green synthesis process remain to be addressed in subsequent studies.

Data Sharing Statement

The corresponding author will provide data that confirms the results of this study upon request.

Acknowledgments

We thank Gabriela Nowak-Wiczk, Dorota Łuszczek and Miłosz Tański for the technical support.

Author Contributions

All authors made a significant contribution to the work reported, whether that is in the conception, study design, execution, acquisition of data, analysis and interpretation, or in all these areas; took part in drafting, revising or critically reviewing the article; gave final approval of the version to be published; have agreed on the journal to which the article has been submitted; and agree to be accountable for all aspects of the work.

Funding

This work was supported by the National Science Center SONATA grant no. UMO-2018/31/D/NZ7/02258 (D.N.) and Faculty of Biology MN Grant no. 539-D140-B164-24 (P.S.).

Disclosure

The authors declare that they have no known competing financial interests or personal relationships that could influence the work reported in this study.

References

1. Naghavi M, Vollset SE, Ikuta KS, et al. Global burden of bacterial antimicrobial resistance 1990-2021: a systematic analysis with forecasts to 2050. *Lancet*. 2024;404(10459):1199–1226. doi:10.1016/S0140-6736(24)01867-1
2. Grooters KE, Ku JC, Richter DM, et al. Strategies for combating antibiotic resistance in bacterial biofilms. *Front Cell Infect Microbiol*. 2024;14:1352273. doi:10.3389/FCIMB.2024.1352273
3. Zhang C, Fang Z, Wang K, Wang J, Wan X. Role of iron in the treatment of sepsis. *Biointerphases*. 2022;19(6). doi:10.1116/6.0003879
4. Sánchez-Jiménez A, Marcos-Torres FJ, Llamas MA. Mechanisms of iron homeostasis in Pseudomonas aeruginosa and emerging therapeutics directed to disrupt this vital process. *Microb Biotechnol*. 2023;16(7):1475–1491. doi:10.1111/1751-7915.14241
5. Frick-Cheng AE, Shea AE, Roberts JR, Smith SN, Ohi MD, Mobley HLT. Iron limitation induces motility in uropathogenic E. coli CFT073 partially through action of LpdA. *mBio*. 2024;15(7). doi:10.1128/MBIO.01048-24
6. Usui M, Yoshii Y, Thiriet-Rupert S, Ghigo JM, Beloin C. Intermittent antibiotic treatment of bacterial biofilms favors the rapid evolution of resistance. *Communications Biology*. 2023;6(1):1–16. doi:10.1038/s42003-023-04601-y
7. Baetke SC, Lammers T, Kiessling F. Applications of nanoparticles for diagnosis and therapy of cancer. *Br J Radiol*. 2015;88(1054):20150207. doi:10.1259/BJR.20150207
8. Stark WJ, Stoessel PR, Wohlleben W, Hafner A. Industrial applications of nanoparticles. *Chem Soc Rev*. 2015;44(16):5793–5805. doi:10.1039/C4CS00362D
9. Khan I, Saeed K, Khan I. Nanoparticles: properties, applications and toxicities. *Arabian Journal of Chemistry*. 2019;12(7):908–931. doi:10.1016/J.ARABJC.2017.05.011

10. Vance ME, Kuiken T, Vejerano EP, McGinnis SP, Hochella MF, Hull DR. Nanotechnology in the real world: redeveloping the nanomaterial consumer products inventory. *Beilstein Journal of Nanotechnology*. 2015;6(1):1769–1780. doi:10.3762/BJNANO.6.181
11. Worldwide Nanomaterials Industry to 2029 - Emerging Applications in the Electronics Industry are Driving Growth - ResearchAndMarkets.com | business Wire. Available from: https://www.businesswire.com/news/home/20210514005289/en/Worldwide-Nanomaterials-Industry-to-2029-Emerging-Applications-in-the-Electronics-Industry-are-Driving-Growth-ResearchAndMarkets.com]. Accessed September 29, 2024.
12. Nam NH, Luong NH. Nanoparticles: synthesis and applications. *Materials for Biomedical Engineering*. 2019;211. doi:10.1016/B978-0-08-102814-8.00008-1
13. Baig N, Kammakakam I, Falath W, Kammakakam I. Nanomaterials: a review of synthesis methods, properties, recent progress, and challenges. *Mater Adv*. 2021;2(6):1821–1871. doi:10.1039/D0MA00807A
14. Krychowiak-Maśnicka M, Wojciechowska WP, Bogaj K, et al. The substantial role of cell and nanoparticle surface properties in the antibacterial potential of spherical silver nanoparticles. *Nanotechnol Sci Appl*. 2024;17:227–246. doi:10.2147/NSA.S489407
15. Ying S, Guan Z, Ofoegbu PC, et al. Green synthesis of nanoparticles: current developments and limitations. *Environ Technol Innov*. 2022;26:102336. doi:10.1016/J.ETI.2022.102336
16. Doyle AA, Stephens JC. A review of cinnamaldehyde and its derivatives as antibacterial agents. *Fitoterapia*. 2019;139. doi:10.1016/J.FITOTE.2019.104405
17. Guo J, Yan S, Jiang X, et al. Advances in pharmacological effects and mechanism of action of cinnamaldehyde. *Front Pharmacol*. 2024;15:1365949. doi:10.3389/FPHAR.2024.1365949
18. Nabavi SF, Di Lorenzo A, Izadi M, Sobarzo-Sánchez E, Daglia M, Nabavi SM. Antibacterial effects of cinnamon: from farm to food, cosmetic and pharmaceutical industries. *Nutrients*. 2015;7(9):7729–7748. doi:10.3390/NU7095359
19. Mateen S, Rehman MT, Shahzad S, et al. Anti-oxidant and anti-inflammatory effects of cinnamaldehyde and eugenol on mononuclear cells of rheumatoid arthritis patients. *Eur J Pharmacol*. 2019;852:14–24. doi:10.1016/J.EJPHAR.2019.02.031
20. Liu Y, An T, Wan D, Yu B, Fan Y, Pei X. Targets and mechanism used by cinnamaldehyde, the main active ingredient in cinnamon, in the treatment of breast cancer. *Front Pharmacol*. 2020;11:1. doi:10.3389/FPHAR.2020.582719
21. Karczewska M, Wang AY, Narajczyk M, Słomiński B, Szalewska-Pałasz A, Nowicki D. Antibacterial activity of t-cinnamaldehyde: an approach to its mechanistic principle towards enterohemorrhagic Escherichia coli (EHEC). *Phytomedicine*. 2024;132. doi:10.1016/J.PHYMED.2024.155845
22. Chen J, Li S, Zheng Q, et al. Preparation of solid lipid nanoparticles of cinnamaldehyde and determination of sustained release capacity. *Nanomaterials*. 2022;12(24):4460. doi:10.3390/NANO12244460
23. Liu Q, Cui H, Muhoza B, et al. Fabrication of low environment-sensitive nanoparticles for cinnamaldehyde encapsulation by heat-induced gelation method. *Food Hydrocoll*. 2020;105:105789. doi:10.1016/J.FOODHYD.2020.105789
24. Sun Q, Cai X, Li J, Zheng M, Chen Z, Yu CP. Green synthesis of silver nanoparticles using tea leaf extract and evaluation of their stability and antibacterial activity. *Colloids Surf a Physicochem Eng Asp*. 2014;444:226–231. doi:10.1016/J.COLSURFA.2013.12.065
25. Salem W, Leitner DR, Zingl FG, et al. Antibacterial activity of silver and zinc nanoparticles against Vibrio cholerae and enterotoxic Escherichia coli. *International Journal of Medical Microbiology*. 2015;305(1):85–95. doi:10.1016/J.IJMM.2014.11.005
26. Aman RM, Zaghloul RA, Saleh NM. Propolis-loaded/dextrose-coated bilosomes for enhanced protection against CCl4-induced liver injury: in vitro and in vivo assessments. *J Drug Deliv Sci Technol*. 2025;107:106756. doi:10.1016/j.jddst.2025.106756
27. Sung HK, Oh SY, Park C, Kim Y. Colorimetric detection of Co2+ ion using silver nanoparticles with spherical, plate, and rod shapes. *Langmuir*. 2013;29(28):8978–8982. doi:10.1021/LA401408F
28. Benzie IFF, Strain JJ. The Ferric Reducing Ability of Plasma (FRAP) as a Measure of "Antioxidant Power": the FRAP Assay. *Anal Biochem*. 1996;239(1):70–76. doi:10.1006/ABIO.1996.0292
29. Gong J. Dissolved Fe(II/III) colorimetric assay using a plate reader (96-well plate) v1. doi:10.17504/protocols.io.bd5fi83n
30. Borowicz M, Krzyżanowska DM, Jafra S. Crystal violet-based assay for the assessment of bacterial biofilm formation in medical tubing. *J Microbiol Methods*. 2023;204:106656. doi:10.1016/J.MIMET.2022.106656
31. Himpsl SD, Mobley HLT. Siderophore detection using chrome azurol S and cross-feeding assays. *Methods in Molecular Biology*. 2019;2021:97–108. doi:10.1007/978-1-4939-9601-8_10
32. Louden BC, Haarmann D, Lynne AM. Use of blue agar CAS assay for siderophore detection. *Journal of Microbiology & Biology Education: JMBE*. 2011;12(1):51. doi:10.1128/JMBE.V12I1.249
33. Kungwani NA, Panda J, Mishra AK, et al. Combating bacterial biofilms and related drug resistance: role of phyto-derived adjuvant and nanomaterials. *Microb Pathog*. 2024;195:106874. doi:10.1016/J.MICPATH.2024.106874
34. Mortazavi-Derazkola S, Yousefinia A, Naghizadeh A, Lashkari S, Hosseinzadeh M. Green synthesis and characterization of silver nanoparticles using elaeagnus angustifolia bark extract and study of its antibacterial effect. *J Polym Environ*. 2021;29(11):3539–3547. doi:10.1007/S10924-021-02122-5
35. Nayak D, Ashe S, Rauta PR, Kumari M, Nayak B. Bark extract mediated green synthesis of silver nanoparticles: evaluation of antimicrobial activity and antiproliferative response against osteosarcoma. *Materials Science and Engineering: C*. 2016;58:44–52. doi:10.1016/J.MSEC.2015.08.022
36. Rodríguez-Carvajal J. Recent advances in magnetic structure determination by neutron powder diffraction. *Physica B Condens Matter*. 1993;192(1–2):55–69. doi:10.1016/0921-4526(93)90108-I
37. Straumanis ME. Neubestimmung der Gitterparameter, Dichten und thermischen Ausdehnungskoeffizienten von Silber und Gold, und Vollkommenheit der Struktur. *Monatsh Chem*. 1971;102(5):1377–1386. doi:10.1007/BF00917194
38. Swanson HE, Fuyat RK, Ugrinic GM. *Standard X-Ray Diffraction Powder Patterns NBC Circular 539 Volume III*. Washington, D.C: United States Department of Commerce National Bureau Of Standards; 1954.
39. Ahmad S, Ahmad S, Ali S, Esa M, Khan A, Yan H. Recent advancements and unexplored biomedical applications of green synthesized Ag and Au nanoparticles: a review. *Int J Nanomedicine*. 2024;19:3187–3215. doi:10.2147/IJN.S453775
40. Bellingeri A, Bertelà F, Burratti L, et al. Detection of Fe(III) ion based on bifunctionalized silver nanoparticles: sensitivity, selectivity and environmental safety. *Mater Chem Phys*. 2024;313:128671. doi:10.1016/J.MATCHEMPHYS.2023.128671
41. Walasek-Janusz M, Grzegorczyk A, Malm A, Nurzyńska-Wierdak R, Zalewski D. Chemical composition, and antioxidant and antimicrobial activity of oregano essential oil. *Molecules*. 2024;29(2):435. doi:10.3390/MOLECULES29020435

42. Hammer KA, Carson CF, Rileya TV. Effects of Melaleuca alternifolia (Tea Tree) essential oil and the major monoterpene component terpinen-4-ol on the development of single- and multistep antibiotic resistance and antimicrobial susceptibility. *Antimicrob Agents Chemother*. 2012;56(2):909. doi:10.1128/AAC.05741-11
43. Yan Y, Xia X, Fatima A, et al. Antibacterial activity and mechanisms of plant flavonoids against gram-negative bacteria based on the antibacterial statistical model. *Pharmaceuticals*. 2024;17(3):292. doi:10.3390/PH17030292
44. Yuan G, Guan Y, Yi H, Lai S, Sun Y, Cao S. Antibacterial activity and mechanism of plant flavonoids to gram-positive bacteria predicted from their lipophilicities. *Scientific Reports*. 2021;11(1):1–15. doi:10.1038/s41598-021-90035-7
45. Ahamad I, Bano F, Anwer R, Srivastava P, Kumar R, Fatma T. Antibiofilm activities of biogenic silver nanoparticles against Candida albicans. *Front Microbiol*. 2022;12:741493. doi:10.3389/FMICB.2021.741493
46. Mikhailova EO. Silver nanoparticles: mechanism of action and probable bio-application. *J Funct Biomater*. 2020;11(4):84. doi:10.3390/JFB11040084
47. Dhaka A, Chand Mali S, Sharma S, Trivedi R. A review on biological synthesis of silver nanoparticles and their potential applications. *Results Chem*. 2023;6:101108. doi:10.1016/J.RECHEM.2023.101108
48. Bruna T, Maldonado-Bravo F, Jara P, Caro N. Silver nanoparticles and their antibacterial applications. *Int J Mol Sci*. 2021;22(13):7202. doi:10.3390/IJMS22137202
49. Anuar AHH, Ghafar SAA, Lim V, Pazli NFAM, Hanafiah RM. Critical evaluation of green synthesized silver nanoparticles-kaempferol for antibacterial activity against methicillin-resistant Staphylococcus aureus. *Int J Nanomedicine*. 2024;19:1339–1350. doi:10.2147/IJN.S431499
50. Kar D, Bandyopadhyay S, Dimri U, et al. Antibacterial effect of silver nanoparticles and capsaicin against MDR-ESBL producing Escherichia coli: an in vitro study. *Asian Pac J Trop Dis*. 2016;6(10):807–810. doi:10.1016/S2222-1808(16)61135-0
51. To D, Massani MB, Coraça-Huber DC, et al. Antibiotic-polyphosphate nanocomplexes: a promising system for effective biofilm eradication. *Int J Nanomedicine*. 2024;19:9707–9725. doi:10.2147/IJN.S473241
52. Karczewska M, Strzelecki P, Bogucka K, Potrykus K, Szalewska-Pałasz A, Nowicki D. Increased Levels of (p)ppGpp correlate with virulence and biofilm formation, but not with growth, in strains of uropathogenic Escherichia coli. *Int J Mol Sci*. 2023;24(4):3315. doi:10.3390/IJMS24043315
53. Strzelecki P, Nowicki D. Tools to study microbial iron homeostasis and oxidative stress: current techniques and methodological gaps. *Front Mol Biosci*. 2025;12. doi:10.3389/fmolb.2025.1628725
54. Holbein BE, Ang MTC, Allan DS, Chen W, Lehmann C. Iron-withdrawing anti-infectives for new host-directed therapies based on iron dependence, the Achilles' heel of antibiotic-resistant microbes. *Environ Chem Lett*. 2021;19(4):2789–2808. doi:10.1007/S10311-021-01242-7
55. Coraça-Huber DC, Dichtl S, Steixner S, Nogler M, Weiss G. Iron chelation destabilizes bacterial biofilms and potentiates the antimicrobial activity of antibiotics against coagulase-negative Staphylococci. *Pathog Dis*. 2018;76(5). doi:10.1093/FEMSPD/FTY052
56. Klebba PE, Newton SMC, Six DA, et al. Iron acquisition systems of gram-negative bacterial pathogens define tonb-dependent pathways to novel antibiotics. *Chem Rev*. 2021;121(9):5193–5239. doi:10.1021/ACS.CHEMREV.0C01005
57. Kontoghiorghes GJ. The importance and essentiality of natural and synthetic chelators in medicine: increased prospects for the effective treatment of iron overload and iron deficiency. *Int J Mol Sci*. 2024;25(9):4654. doi:10.3390/IJMS25094654
58. Wen Z, Zhao Y, Gong Z, et al. The mechanism of action of ginkgolic acid (15:1) against gram-positive bacteria involves cross talk with iron homeostasis. *Microbiol Spectr*. 2022;10(1). doi:10.1128/SPECTRUM.00991-21
59. AAlikhani M, Jahanshahi M, Khalili M. The natural iron chelators' ferulic acid and caffeic acid rescue mice's brains from side effects of iron overload. *Front Neurol*. 2022;13. doi:10.3389/FNEUR.2022.951725
60. Eslami S, Ebrahimzadeh MA, Biparva P. Green synthesis of safe zero valent iron nanoparticles by Myrtus communis leaf extract as an effective agent for reducing excessive iron in iron-overloaded mice, a thalassemia model. *RSC Adv*. 2018;8(46):26144–26155. doi:10.1039/C8RA04451A
61. Leitão MM, Gonçalves ASC, Moreira J, et al. Unravelling the potential of natural chelating agents in the control of Staphylococcus aureus and Pseudomonas aeruginosa biofilms. *Eur J Med Chem*. 2025;283:117163. doi:10.1016/J.EJMECH.2024.117163
62. Itoh K, Tsutani H, Mitsuke Y, Iwasaki H. Potential additional effects of iron chelators on antimicrobial- impregnated central venous catheters. *Front Microbiol*. 2023;14. doi:10.3389/FMICB.2023.1210747
63. Stickler DJ. Clinical complications of urinary catheters caused by crystalline biofilms: something needs to be done. *J Intern Med*. 2014;276(2):120–129. doi:10.1111/JOIM.12220
64. Tantawy MA, Sultan EY, Elsabbagh HM, Saleh NM. Pivotal roles of polymeric nanoparticles in modulating intestinal permeability, improving stability, and rediscovering antivirulence activity of nitrofurantoin. *J Drug Deliv Sci Technol*. 2025;104:106578. doi:10.1016/j.jddst.2024.106578
65. Goda RM, El-Baz AM, Khalaf EM, Alharbi NK, Elkhooly TA, Shohayeb MM. Combating bacterial biofilm formation in urinary catheter by green silver nanoparticle. *Antibiotics*. 2022;11(4):495. doi:10.3390/ANTIBIOTICS11040495
66. Prateeksha P, Bajpai R, Rao CV, Upreti DK, Barik SK, Singh BN. Chrysophanol-functionalized silver nanoparticles for anti-adhesive and anti-biofouling coatings to prevent urinary catheter-associated infections. *ACS Appl Nano Mater*. 2021;4(2):1512–1528. doi:10.1021/ACSANM.0C03029
67. Chadha J, Thakur N, Chhibber S, Harjai K. A comprehensive status update on modification of foley catheter to combat catheter-associated urinary tract infections and microbial biofilms. *Crit Rev Microbiol*. 2024;50(2):168–195. doi:10.1080/1040841X.2023.2167593
68. Batista AFP, Rosa LCM, Pizzo JS, et al. Biogenic silver nanoparticles and cinnamaldehyde as an effective sanitizer for fresh sweet grape tomatoes. *J Food Sci Technol*. 2023;60(9):2477–2485. doi:10.1007/S13197-023-05770-8
69. Prasastha Ram V, Yasur J, Abishad P, et al. Antimicrobial efficacy of green synthesized nanosilver with entrapped cinnamaldehyde against multi-drug-resistant enteroaggregative Escherichia coli in Galleria mellonella. *Pharmaceutics*. 2022;14(9):1924. doi:10.3390/PHARMACEUTICS14091924
70. Ghosh IN, Patil SD, Sharma TK, Srivastava SK, Pathania R, Navani NK. Synergistic action of cinnamaldehyde with silver nanoparticles against spore-forming bacteria: a case for judicious use of silver nanoparticles for antibacterial applications. *Int J Nanomedicine*. 2013;8(1):4721–4731. doi:10.2147/IJN.S49649